Back-Hopping in Ultra-Scaled MRAM Cells

M. Bendra*,**, S. Fiorentini*,**, J. Ender*,**, R.L. de Orio**, T. Hadámek*,
N.P. Jørstad*, B. Pruckner*, S. Selberherr**, W. Goes†, and V. Sverdlov*,**

* Christian Doppler Laboratory for Nonvolatile Magnetoresistive Memory and Logic at the
** Institute for Microelectronics, TU Wien, Gußhausstraße 27-29, A-1040 Wien, Austria
† Silvaco Europe Ltd., Compass Point, St Ives, Cambridge, PE27 5JL, United Kingdom
e-mail: bendra@iue.tuwien.ac.at

Abstract—**The development of advanced magnetic tunnel junctions with a footprint in the single-digit nanometer range can be achieved using an elongated multilayer ferromagnetic free layer structure. Using the spin drift-diffusion model, we investigated the back-hopping effect in ultra-scaled STT-MRAM devices. Unwanted switching of the middle-layer structure has been identified as a possible cause of the back-hopping effect, which leads to a writing error in the magnetization state of the free layers. To understand the switching of the free layer, the torque acting on both parts of the composite free layer is studied in detail. A reduction in the size of MRAM components to increase the memory density leads to lower anisotropies and thus increases the likelihood of back-hopping due to the presented mechanism. A possible solution to avoid erroneous switching is to increase the magnetic anisotropy of the layers.**

Keywords—*Back-Hopping, Spin Transfer Torques, Ultra-Scaled MRAM Cells, Perpendicular Magnetic Anisotropy, Writing Error*

I. INTRODUCTION

Emerging nonvolatile spin-transfer torque (STT) magnetoresistive random access memories (MRAM) have generated significant interest because of their high speed, and endurance. Thus, they are attractive for Computing-in-Memory concepts [1], embedded automotive [2], low-latency industrial applications [3], last-level cache [4], and high density MRAM arrays [5]. An STT-MRAM cell is based on a magnetic tunnel junction (MTJ) with perpendicular magnetic anisotropy (PMA) and is composed of several layers, including a CoFeB reference layer (RL) and a free magnetic layer (FL) separated by an MgO tunnel barrier (TB), which form the MTJ. To increase the PMA, the FL, typically composed of two CoFeB layers and a thin metal buffer, is interfaced with a second MgO layer [6]. Introducing more MgO layers [7] and elongating the FL allows to boost the perpendicular anisotropy while reducing the FL diameter [8]. A further reduction in the size of MRAM components to increase the memory density leads to lower anisotropies and thus increases the likelihood of erroneous switching. At high currents running through a cell the erroneous switching can occur due to an unwanted flip of the RL, or back hopping [9]. For the accurate design of ultra-scaled MRAM cells (Fig. 1) it is paramount to understand the magnetization dynamics of magnetic materials related to the performance of MTJs.
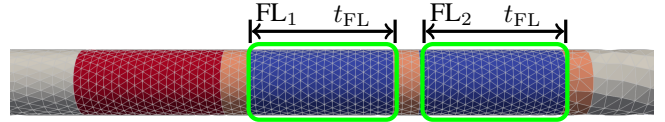

Figure 1: Simplified mesh of the simulated ultra-scaled MRAM cell. This composite structure consists of a CoFeB (5)|MgO (0.9)|CoFeB (5)|MgO (0.9)|CoFeB (5)|MgO (0.9) MTJ connected to normal metal contacts (50), where the numbers in parentheses indicate the thickness of each layer in nanometer. The diameter is $2.3\,\text{nm}$. A bias of $1.5\,\text{V}$ is applied across the structure. The color coding represents the following: red for the RL, blue for the FL, orange for the TB, and gray for the non-magnetic contacts. The green framed section denotes the FL segments for FL_1 and FL_2, with the length t_{FL}.

II. MICROMAGNETICS MODEL

We developed a fully three-dimensional finite element method (FEM) based modeling and simulation approach which includes all relevant physical phenomena, (described in equations (1)-(6)) [10], responsible for proper ultra-scaled MRAM operation. We numerically solve the magnetization dynamics, described by the Landau-Lifshitz-Gilbert equation (LLG) (1).

$$\frac{\partial \mathbf{m}}{\partial t} = -\gamma \mathbf{m} \times \mathbf{H}_{\text{eff}} + \alpha \mathbf{m} \times \frac{\partial \mathbf{m}}{\partial t} + \frac{1}{M_S}\mathbf{T_S} \quad (1)$$

The effective field $\mathbf{H}_{\text{eff}}$ accounts for the magnetic anisotropy field, the exchange field, as well as the demagnetization field. The latter contribution to $\mathbf{H}_{\text{eff}}$ is evaluated only on the disconnected magnetic domain by using a hybrid approach combining the boundary element method and the finite element method [11]. To appropriately model the switching of ultra-scaled MRAM cells, the torque $\mathbf{T_S}$ is described by the following equation:

$$\mathbf{T_S} = -\frac{D_e}{\lambda_J^2}\mathbf{m} \times \mathbf{S} - \frac{D_e}{\lambda_\varphi^2}\mathbf{m} \times (\mathbf{m} \times \mathbf{S}). \quad (2)$$

The coupled spin and charge drift-diffusion method, as defined by equations (3)-(5), accurately describes the charge and the spin transport through a nanometer-sized magnetic valve [12].

$$D_e\left(\frac{\mathbf{S}}{\lambda_{sf}^2} + \frac{\mathbf{S} \times \mathbf{m}}{\lambda_J^2} + \frac{\mathbf{m} \times (\mathbf{S} \times \mathbf{m})}{\lambda_\varphi^2}\right) = -\boldsymbol{\nabla} \cdot \mathbf{J_S} \quad (3)$$

$$\mathbf{J_S} = -\frac{\mu_B}{e}\beta_\sigma\big(\mathbf{J_C} \otimes \mathbf{m}+$$

$$+\beta_D D_e \frac{e}{\mu_B}[(\boldsymbol{\nabla}\mathbf{S})\mathbf{m}] \otimes \mathbf{m}\big) - D_e\boldsymbol{\nabla}\mathbf{S} \quad (4)$$

Table I: Simulation Parameters.

Parameter	Value
Gilbert damping, α	0.015
Gyromagnetic ratio, γ	$1.76 \cdot 10^{11} \frac{\text{rad}}{\text{s} \cdot \text{T}}$
Saturation magnetization, M_S	$1.2 \cdot 10^{6} \frac{\text{A}}{\text{m}}$
Exchange constant, A	$1 \cdot 10^{-11} \frac{\text{J}}{\text{m}}$
Free layer length, t_{FL}	X nm
Interface anisotropy, K_i	$1.53 \cdot 10^{-3} \frac{\text{J}}{\text{m}^2}$
Uniaxial anisotropy constant, K	K_i/t_{FL}
Current spin polarization, β_σ	0.7
Diffusion spin polarization, β_D	1.0
Electron diffusion coefficient, D_e	$2 \cdot 10^{-2} \frac{\text{m}^2}{\text{s}}$
Spin-flip length, λ_{sf}	10 nm
Exchange length, λ_J	1 nm
Spin dephasing length, λ_φ	0.4 nm
Electrical resistance in the anti-parallel state, R_{AP}	750 kΩ
Electrical resistance in the parallel state, R_P	410 kΩ

$$\mathbf{J_C} = \sigma \mathbf{E} - \beta_D D_e \frac{e}{\mu_B}[(\boldsymbol{\nabla}\mathbf{S})\mathbf{m}] \quad (5)$$

We extended this method to MTJs by modeling the TB as a poor conductor (6) with a local resistance dependent on the relative orientation of the FL magnetization [10].

$$\sigma(\theta) = \frac{\sigma_P + \sigma_{AP}}{2}\left(1 + \left(\frac{\text{TMR}}{2+\text{TMR}}\right)\cos\theta\right) \quad (6)$$

$\sigma_{P(AP)}$ is the conductivity in the parallel (anti-parallel) state, θ is the angle of the FL direction with respect to the RL one. The tunneling magnetoresistance TMR $= G_P - G_{AP}/G_{AP}$, where $G_{P(AP)}$ is the conductance in the parallel (anti-parallel) state. The tunneling spin current polarization taken from [10] is introduced by applying appropriate magnetization dependent boundary conditions at the left and right interface of the tunneling layers.

III. RESULTS

The following sections report the results of switching simulations performed in the structure depicted in Fig. 1. The parameters employed are presented in Table I. They are consistent with CoFeB and MgO for the FM layers and TB layers, respectively. The low values of λ_J and λ_φ are employed to have complete absorption of the transverse spin accumulation components in the FL near the TB interface [10]. The tunneling spin current polarization creates a jump between the values of the spin accumulation at the left and right interface of the TB. This is the manifestation of the MTJ polarization effects on the spin current. The transverse spin accumulation is quickly absorbed, resulting in torques that are acting near the TB|FL interface.

In Fig. 2 the magnetization trajectories for the switching from anti-parallel (AP) to parallel (P) and from P to AP of an ultra-scaled MRAM with different FL configurations are displayed. The FL configuration is either symmetric or antisymmetric. The parts of the FL can be equal or different. In Fig. 2 bold lines represent a symmetric configuration, for dashed lines with triangles, the first FL_1 length is fixed with 5 nm and the second FL_2 is varied to be 2 nm, 3 nm, and 4 nm, respectively. For dotted lines with crosses, the reverse is the case: FL_2 is fixed with 5 nm, and FL_1 is varied. The applied bias is 1.5 V or -1.5 V depending on the magnetization switching direction, P to AP, or AP
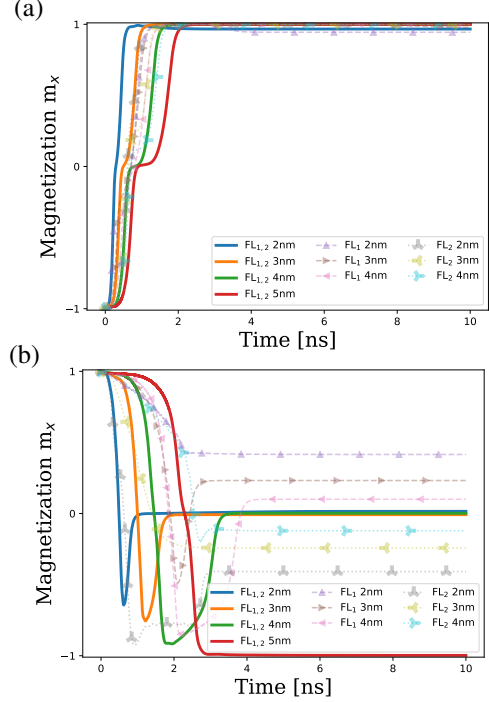
(a)

(b)

Figure 2: Magnetization trajectories for the switching from (a) AP to P and (b) P to AP for different combinations of FL lengths. The solid line represents a symmetric configuration where both FL have the same length. The dotted line and the dashed line correspond to an asymmetric structure. In the former, the first FL layer is fixed, the second is varied, and in the latter, the second FL layer is fixed, and the first FL layer is varied. The polarization of the TB used is 0.6, 0.5, and 0.2, in order from left to right in Fig. 1.

to P. Fig. 2(a) reports, that the successful switching of the FL from AP to P is always obtained. Fig. 2(b) shows that successful switching from P to AP is only obtained for the symmetric configuration and a larger length t_{FL} of 5 nm. The difference between the intermediate states of the dashed and dotted lines comes from the different lengths, and therefore, the magnetizations of the FL_1 and FL_2 resulting in the distinct total magnetization of the FL in the final state.

The differences in the response times of the cells are due to the different uniaxial anisotropies, which depend on the length of the layer. A shorter layer possesses a reduced energy barrier separating the two magnetization configurations, so that the speed of the response times is improved in the case of the shorter layer.

In Fig. 3 we report switching realizations where we modeled the polarization of the TBs, such that the TB in the middle of the FL is the higher one. Higher TB polarization leads to higher spin current so that the torque acting on the two FL segments is stronger than the torque acting on RL and FL_1. In Fig. 3(a), all structures switch successfully except for the symmetric configuration with an FL length of 2 nm. Here, the magnetization develops a single oscillation before reaching a stable state. This is due to the weak anisotropy, and the torques from FL_2 acting on FL_1 being more substantial than from RL, leading
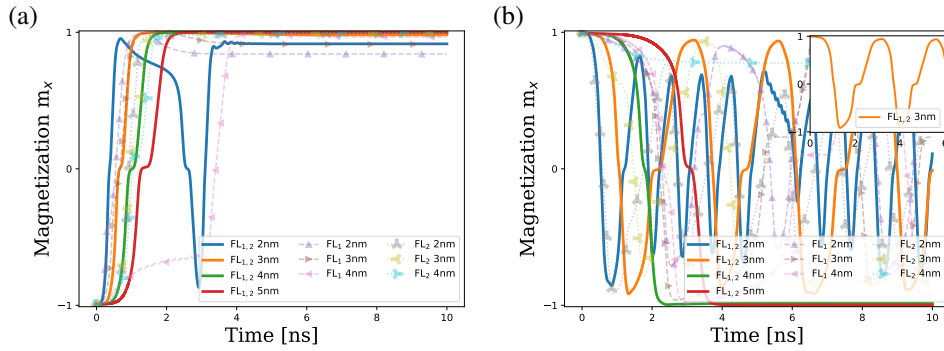
Figure 3: Magnetization trajectories for the switching from (a) AP to P and (b) P to AP for different combinations of FL lengths, were the same methodology as in Fig. 2 was applied, but with increasing polarization of TB in the middle of the FL. In addition, the symmetrical structure with 3 nm thick FLs is highlighted in the inset. The polarization of the TB used is 0.5, 0.9, and 0.2, in order from left to right in Fig. 1
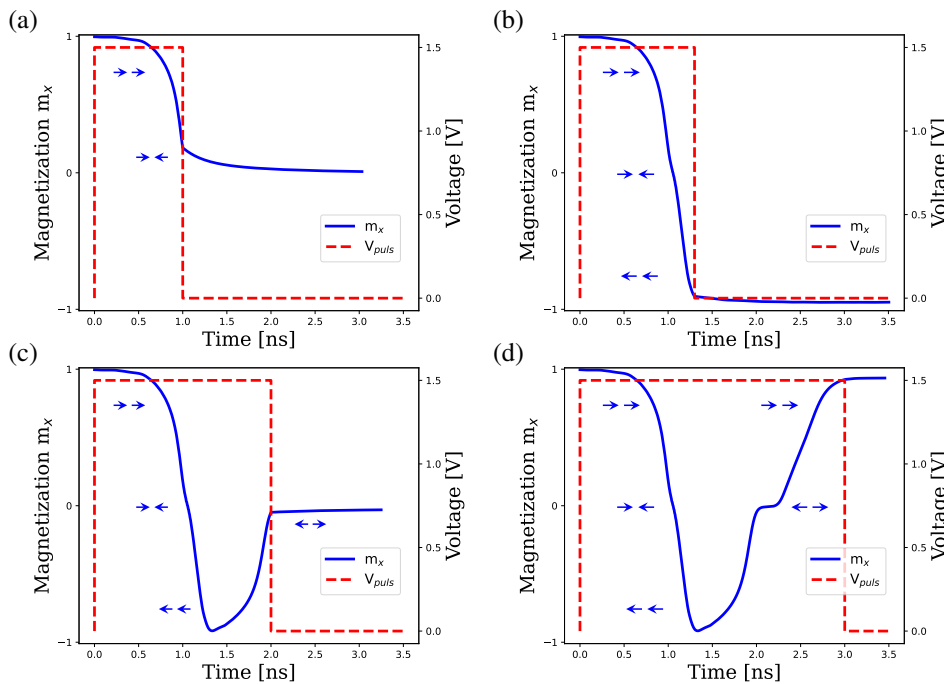

Figure 4: Magnetization trajectories for a symmetric structure with 3 nm thick FLs, switching from P to AP for different duration of the applied bias. The solid blue line represents the x-component of the magnetization and the red dashed line the duration and amplitude of the bias pulse. The arrows along the magnetization represent the state of FL_1 and FL_2.

to an initial back-and-forth switching before reaching the final state. Fig. 3(b) illustrates the back-hopping effect. As reported in the inset, the structure with 3 nm shows continuous transitions between the sequence of states as long as the current is applied. The sequential switching procedure of the composite FL is as follows: The torque acting from FL_2 to FL_1 is opposite to that of the RL, so FL_2 switches first. After FL_2 switches, the torque contributions from FL_2 and the RL act on FL_1 in the same sense flipping FL_1 and completing the switching.

As the bias is maintained, the magnetization of FL_2 reverses due to the higher polarization in the middle TB and the back-hopping effect of FL_2 occurs. The torques from the RL favor the anti-parallel state and those from FL_2 favor the parallel state. However, due to the higher polarization in the middle TB, the torques from FL_2 are

stronger than those from the RL, so FL_1 flips, and the whole FL returns to the initial configuration. This process repeats as long as the bias is maintained.

In Fig. 4 we report switching realizations with different durations of the applied bias. If we adjust and vary the duration of the bias pulse, we can realize a multi-level cell with four different states. These states of the FL are illustrated by the blue arrows and follow the same switching procedure as mentioned earlier. By properly modulating the duration of the pulse, all four states can be addressed. A distinction between the two intermediate states can be recognized by the fact that the first state FL_1 parallel to the RL and anti-parallel to FL_2 has a lower resistance than the state with FL_1 anti-parallel to the RL and FL_2. Fig. 5 demonstrates the snapshots of the important stages of the switching sequence for the AP
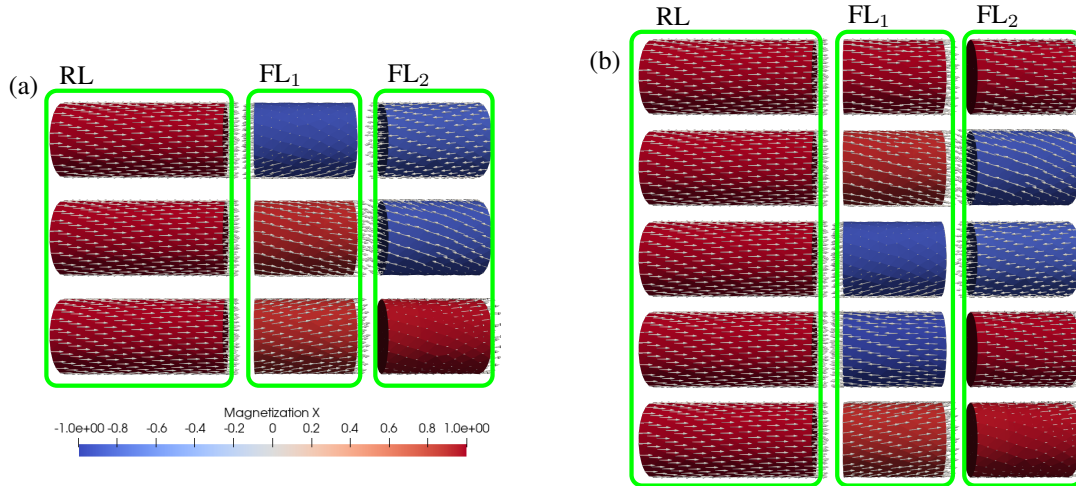
Figure 5: Switching snapshot of MRAM cell's in the following order: Initial, intermediate and final state, for the configuration (a) AP to P and (b) P to AP. Arrows indicate the magnetization directions, and color-coding represents the average magnetization in x-direction. Depending on the switching direction, a negative bias for (a) or a positive bias for (b) is applied. To achieve the respective states, the pulse duration is modulated as shown in the previous Fig. 4.

to P and P to AP process. Fig. 5(b) displays the arrow configuration of Fig. 4. To get from the configuration in Fig. 3(a) or Fig. 3(c) back to the desired AP or P configuration, only a short bias pulse is necessary to reset the structure into the desired state.

IV. CONCLUSION

The drift-diffusion approach is supplemented with appropriate boundary conditions for the spin current $\mathbf{J_S}$ at the TB interfaces to account for the dependence of the torque on the relative magnetization orientation specific to MTJs. The boundary condition is key to describe the spin current and the spin accumulations in the RL and FL. This gives us the opportunity to describe the spin and charge transport coupled to the magnetization in arbitrary stacks of MTJs. We demonstrated an appearance of the back-hopping effect in ultra-scaled STT-MRAM devices with a composite free layer. By proper analysis of the back-hopping effect, we demonstrated the potential of employing this effect to engineer devices as a multi-bit cells with four different states.

REFERENCES

[1] S. Jung, H. Lee, S. Myung, H. Kim, S. K. Yoon, S.-W. Kwon, Y. Ju, M. Kim, W. Yi, S. Han, and et al., "A crossbar array of magnetoresistive memory devices for in-memory computing," *Nature*, vol. 601, no. 7892, p. 211–216, 2022.

[2] V. B. Naik, K. Yamane, T. Lee, J. Kwon, R. Chao *et al.*, "Jedec-qualified highly reliable 22nm FD-SOI embedded MRAM for low-power industrial-grade, and extended performance towards automotive-grade-1 applications," in *IEEE International Electron Devices Meeting (IEDM)*, 2020, pp. 11.3.1–11.3.4.

[3] S. Ikegawa, K. Nagel, F. B. Mancoff, S. M. Alam, M. Arora, M. DeHerrera, H. K. Lee, S. Mukherjee, G. Shimon, J. J. Sun, I. Rahman, F. Neumeyer, H. Y. Chou, C. Tan, A. Shah, and S. Aggarwal, "High-speed (400MB/s) and low-BER STT-MRAM technology for industrial applications," in *International Electron Devices Meeting (IEDM)*, 2022, pp. 10.4.1–10.4.4.

[4] G. Hu, C. Safranski, J. Z. Sun, P. Hashemi, S. L. Brown, J. Bruley, L. Buzi, C. P. D'Emic, E. Galligan, M. G. Gottwald, O. Gunawan, J. Lee, S. Karimeddiny, P. L. Trouilloud, and D. C. Worledge, "Double spin-torque magnetic tunnel junction devices for last-level cache applications," in *International Electron Devices Meeting (IEDM)*, 2022, pp. 10.2.1–10.2.4.

[5] S. M. Seo, H. Aikawa, S. G. Kim, T. Nagase, Y. Ito, T. J. Ha, K. Yoshino, B. K. Jung, T. Oikawa, K. Y. Jung, H. I. Moon, B. S. Kim, F. Matsuoka, K. Hatsuda, K. Hoya, S. Kim, S.-H. Lee, M.-H. Na, and S. Y. Cha, "First demonstration of full integration and characterization of 4f² 1s1m cells with 45 nm of pitch and 20 nm of mtj size," in *International Electron Devices Meeting (IEDM)*, 2022, pp. 10.1.1–10.1.4.

[6] H. Sato, M. Yamanouchi, S. Ikeda, S. Fukami, F. Matsukura, and H. Ohno, "MgO/CoFeB/Ta/CoFeB/MgO recording structure in magnetic tunnel junctions with perpendicular easy axis," *IEEE Transactions on Magnetics*, vol. 49, no. 7, pp. 4437–4440, 2013.

[7] K. Nishioka, H. Honjo, S. Ikeda, T. Watanabe, S. Miura *et al.*, "Novel quad interface MTJ technology and its first demonstration with high thermal stability and switching efficiency for STT-MRAM beyond 2Xnm," in *Symposium on VLSI Technology*, 2019, pp. T120–T121.

[8] B. Jinnai, J. Igarashi, K. Watanabe, T. Funatsu, H. Sato *et al.*, "High-performance shape-anisotropy magnetic tunnel junctions down to 2.3 nm," in *IEEE International Electron Devices Meeting (IEDM)*, 2020, pp. 24.6.1–24.6.4.

[9] C. Abert, H. Sepehri-Amin, F. Bruckner, C. Vogler, M. Hayashi, and D. Suess, "Back-hopping in spin-transfer-torque devices: Possible origin and countermeasures," *Physical Review Applied*, vol. 9, p. 054010, 2017.

[10] S. Fiorentini, M. Bendra, J. Ender, R. L. de Orio, W. Goes, S. Selberherr, and V. Sverdlov, "Spin and charge drift-diffusion in ultra-scaled mram cells," *Sci. Rep.*, vol. 12, no. 1, 2022.

[11] J. Ender, M. Mohamedou, S. Fiorentini, R. Orio, S. Selberherr, W. Goes, and V. Sverdlov, "Efficient demagnetizing field calculation for disconnected complex geometries in STT-MRAM cells," in *International Conference on Simulation of Semiconductor Processes and Devices (SISPAD)*, 2020, pp. 213–216.

[12] C. Petitjean, D. Luc, and X. Waintal, "Unified drift-diffusion theory for transverse spin currents in spin valves, domain walls, and other textured magnets," *Phys. Rev. Lett.*, vol. 109, p. 117204, 2012.